Article

Measured Rogue Waves and Their Environment

Mark D. Orzech * and David Wang

Naval Research Lab, 1009 Balch Blvd, Stennis Space Ctr, MS 39529, USA; david.wang@nrlssc.navy.mil
* Correspondence: mark.orzech@nrlssc.navy.mil; Tel.: +1-228-688-5974

Abstract: We conduct a comprehensive analysis of over 350 years of accumulated ocean surface elevation time series and examine evidence for the effects of nonlinear frequency modulation, wave directional spread, surface current shear, and wind forcing on the likelihood of rogue wave development. Hourly sections of positional time series from 34 surface buoys are examined to identify over 8000 rogue wave events, recording wave sizes, times of occurrence, and geographic locations. The initial dataset is subjected to a quality control process to identify and remove false positives. We investigate the correlation of rogue events with the specified marine environmental factors in an attempt to validate the predictions of earlier theoretical and modeling analyses. The rogue event dataset is contrasted with a control, non-rogue dataset containing a total of nearly 510,000 hourly data segments of surface wave data. The analysis combines the wave records with surface current and wind data from state-of-the-art global coupled models. Statistics of the identified rogue events are summarized, and results of the environmental factor analysis are presented and discussed. This study finds some support for a causal connection between each of the environmental factors and the development of rogue waves. Results also suggest that localized environmental conditions at specific sites, such as seasonal variations in directional spread and/or high surface current vorticity, may provide useful signals of greater rogue wave threat.

Keywords: rogue waves; waverider buoys; wave-current interaction; spectra; surface wind forcing

1. Introduction

Rogue waves in the ocean environment are normally defined as surface waves that are anomalously large relative to other waves in the nearby region at a given time. Common criteria for a wave to be considered rogue are that its height be greater than twice the local significant wave height ($H_r > 2H_s$), or that its crest elevation above sea level be at least 25% larger ($\eta_r > 1.25H_s$), where H_s is the average height of the largest third of waves in the local environment [1–3].

It is generally accepted that rogue waves do occur occasionally in the global ocean. However, there is still some uncertainty as to whether these relatively extreme features are generated by specific and predictable environmental conditions or are instead merely statistically justifiable events occurring no more often than would be expected based on a standard Rayleigh wave height distribution. Theoretical, experimental, and numerical investigations over the past several decades have provided evidence for the former ("causal factor") hypothesis, examining in particular the effects of nonlinear frequency modulation, wave directional distribution, surface currents, and winds on rogue wave development (e.g., [1,4]). While there is considerable evidence from lab and theory that rogue waves can be produced by frequency modulation in wave spectra for unidirectional waves (e.g., [2,5]), these effects are expected to be reduced in the open ocean. The Benjamin Feir Index (BFI [2]) is a common measure of such wave nonlinearity, with larger BFI indicating a higher likelihood for rogue wave occurrence. Theoretical and lab studies in three-dimensional (3D) domains have also pointed to the importance of the wave

directional distribution, showing frequency modulation and rogue wave likelihood to be greater for directionally narrow wave spectra [6,7].

There is also reasonably strong support from lab, theory, and models for the proposition that horizontal surface current shear and wind forcing can each act to modulate a wave spectrum, depending on their direction and magnitude relative to the waves. Manolidis et al. [8] and Onorato et al. [9], among others, show that a negative horizontal shear in a current opposing the wave direction, with current magnitude increasing as the waves propagate into it, can foster rogue wave development. Unpublished additional analysis by Manolidis and others also provides evidence that a negative horizontal shear in a current traveling with a wave group can also promote rogue wave growth (see [10]).

Recent modeling work by Simeonov et al. (pers. comm.) and earlier theoretical work [1,11–13] suggest that nonlinear wave states can be effectively dampened by strong winds blowing in the same direction as the dominant waves. Specifically, authors in [13] suggest that such dampening will occur for 10 m wind velocity U_{10} in the range $4c < U_{10} < 8c$, where c is the phase speed of monochromatic waves, and authors in [1] predict that similar damping will occur under hurricane conditions (i.e., $U_{10} < 33$ m/s). Extending that result, Simeonov et al. also find that opposing winds of moderate strength (i.e., $U_{10} \sim c_p$, where c_p = phase speed of peak wave) can increase the nonlinearity of such wave states. In contrast, Fedele et al. [14] and others have argued that nonlinear modulation is not a significant factor in most rogue wave development. Adcock et al. [15] analyze conditions associated with the famous 1995 "Draupner" rogue wave and conclude that it resulted primarily from crossing long waves and second order nonlinear effects, with little contribution from nonlinear wave–wave modulation effects. Babariol et al. [16] have implemented a purely statistical method for predicting space–time extreme wave height ranges, based on the quasi-determinism theory of Boccotti [17].

Datasets of actual measured rogue wave events, in combination with concurrent ocean and atmospheric data, can play an important role in helping to confirm or refute the hypothesized effects of various environmental causal factors in the field and/or provide support for statistical estimates of extreme waves. Several authors have attempted to catalog significant rogue wave events from credible media reports (e.g., [18,19]), facilitating follow-up studies to investigate the specific conditions associated with selected events. One such event, the sinking of the El Faro freighter in 2015, is examined by [20], who initialize a time-dependent model with sea state data from Hurricane Joaquin. They comment that the ship was more likely to meet a rogue wave while in transit than it would have been if at a fixed point, and that local wind gustiness and wave breaking likely affected the magnitude of any rogues the ship did encountered. It is important to note that epistemic uncertainties in such model-based estimates of rogue wave likelihood may be increased in hurricane-dominated regions, to the point where the uncertainties exceed the differences between competing models [21].

Benetazzo et al. [22] use a stereo camera system on an oceanic platform in the Adriatic Sea to record surface elevations for a roughly 3000 m^2 region over a 15 h period with mature waves ($H_s \sim$ 1–2 m). Surprisingly, they identify 16 rogue waves (with heights exceeding $2H_s$) in the images during this relatively short time, the largest of which has $H_r \approx 3$ m $\approx 2.2H_s$. Over 3600 rogues were identified in wave gauge data from oil platforms by [23], who then found that these events were uncorrelated with averages of environmental conditions such as sea state, wind forcing, or current direction/magnitude. Cavaleri et al. [24] track depth-limited extreme waves in detailed data records from a 2018 storm near Italy, suggesting that the storm itself belonged to a "different family of events." Fedele et al. [25] analyze measured wave data from two storms in intermediate water depths, concluding that nonlinear dispersion effects generally cause waves to break before reaching rogue crest heights, and finding that second order bound nonlinearities (rather than third-order resonant modulation effects) were the dominant contributors to wave growth in the storms. Very large waves of heights 20 m or more have been measured during other hurricanes and large storms (e.g., [26,27]), but because of the generally extreme conditions in the local environment ($H_s \sim$ 10–15 m), they did not meet the criterion for rogue waves.

The Coastal Data Information Program (CDIP) at U.C. San Diego maintains an extensive fleet of Waverider surface buoys [28] at both coastal and open ocean locations, many of which record their positional time series at subsecond intervals. Baschek and Imai [3] analyzed data from 16 of these buoys along the U.S. west coast, identifying over 7000 rogue waves in 81 years of buoy surface time series. The Baschek and Imai analysis was extended to 80 buoy sites in [29], in which the general conclusion was reached that the frequency of rogue wave occurrence is spatially variable and depends on specific sea state characteristics at any given location.

The present investigation utilizes surface wave elevation time series from 34 intermediate- to deep-water CDIP buoys to identify and tabulate measured rogue wave events, with a procedure similar to that in [3] and [29]. Like some previous investigations, we examine correlations of events with BFI and directional spread of the wave spectra. Here, however, we also supplement our rogue event results with (model-generated) surface current and wind fields to examine the correlation between rogue wave occurrence and the direction and magnitude of current shear and near surface wind vectors. We compare results for the rogue event data with a larger non-rogue "control" dataset, examining statistics for both the full datasets and smaller selections corresponding to more intense and focused sea states. This effort aims to use field data to test the model-based results of [8] and [9] described above, as well as the preliminary findings on wind effects of [13] and Simeonov et al. We ultimately do find a limited degree of positive correlation between rogue wave events and each of the identified causal factors (i.e., BFI, directional spreading, current shear, and wind), with some factors more strongly correlated than others.

The article is organized as follows: Section 2 describes the wave, current, and wind datasets utilized for the study and the manner in which they were processed. Section 3 summarizes the results of the analysis and the levels of correlation achieved between rogue events and wave statistics, current shear, and winds under a range of conditions. Section 4 provides further discussion of these results and summarizes the overall conclusions of the study.

2. Data Sources and Analysis Methods

Surface wave elevation and horizontal displacement time series were obtained for varying time ranges (2–20 years) from 34 Datawell Waverider buoys maintained by CDIP (https://cdip.ucsd.edu). The wave buoys record their position at roughly 1.28 Hz (dt = 0.78 s). A typical swell wave (with period T ~ 10 s), would thus be described by approximately 13 points. Details including geographic location, depth, time range of the dataset, and the number of years analyzed are summarized in Table A1 (all tables are located in the Appendix). Twenty buoys are located along the U.S. west coast, with twelve further out in the Pacific, one in the Gulf of Mexico, and one off the U.S. east coast (Figure 1). All buoys are in depths exceeding 75 m. Rogue events were identified by dividing each buoy's elevation dataset into one-hour sections, identifying all individual waves via the zero-upcrossing method, determining significant wave height, H_s, as the average of the largest third of the waves, and marking any wave whose height equaled or exceeded $2 \cdot H_s$ for a given one-hour section. For each data sample, a maximum of one rogue wave was recorded by selecting only the single largest wave that met the criterion. The larger non-rogue "control" dataset was compiled from wave statistics at each buoy location for every hourly time step that did not include a rogue wave event.

Quality control measures were applied to all datasets to eliminate false events caused by instrument error, electronic spikes, and other unidentified glitches. These measures included limits on acceptable wave elevation kurtosis ($2 < \kappa < 6$), surface acceleration ($\partial^2[x, y, z]/\partial t^2 < g$), and maximum horizontal buoy excursion ($[\Delta x, \Delta y] < 1.8 \cdot H_{s,[x,y]}$), as well as elimination of overly extreme wave crests ($\eta_c < 1.5 \cdot H_s$). In these criteria, x, y, and z are east, north, and vertical buoy displacements, respectively, $H_{s,[x,y]} = 4$ times standard deviation of buoy displacement time series in the (x,y) dimension, and g = 9.81 m/s^2. Only events with rogue wave height $H_r > 1$ m were included. When more than one rogue wave was identified in a one-hour time series, the data were visually inspected, and any with obviously unrealistic behavior (e.g., two separate rogue waves of the exact same crest height) were excluded.

Basic details about identified rogue events at each buoy are summarized in Table A2. Following QC measures, the rogue event dataset contained a total of 8013 separate entries, while the non-rogue dataset contained 507,802 entries.
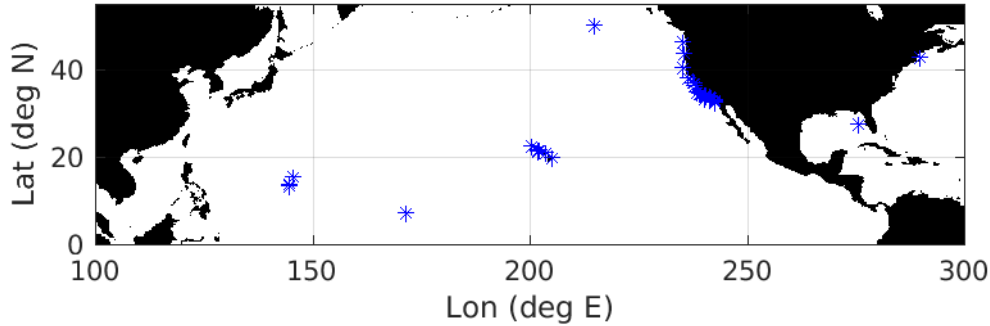
Figure 1. Locations of 34 analyzed Datawell buoys (blue asterisks).

Ocean surface current data at 0.08° resolution were obtained from the GOFS3.1 1/12° global reanalysis ([30]; https://www.hycom.org). The reanalysis consisted of HYCOM simulations with NCODA-based data assimilation and 41 depth layers. The surface currents in this analysis were represented by the first layer of the model reanalysis (depth = 0–2 m). Current shear components along the two Cartesian axes were computed for every time step at the 34 buoy locations as

$$\delta u = \overline{u}_E - \overline{u}_W \tag{1}$$

$$\delta v = \overline{v}_N - \overline{v}_S \tag{2}$$

where the vector velocity $\vec{U} = u\hat{i} + v\hat{j}$ has components u (positive eastward) and v (positive northward) and the spatial averages $\overline{u}_E, \overline{u}_W, \overline{v}_N, \overline{v}_S$ were each calculated using surface current data from the eight points (of a 16-point square) that were located immediately to the E, W, N, and S of the wave buoy coordinates (Figure 2). The shear components δu and δv were computed over mean separation distances equal to two times the grid spacing (i.e., 0.16°) and have units of *m/s/*°. The current shear along the axis of the peak wave direction was computed as the sum of the two component contributions:

$$\delta U_p = \delta u_p + \delta v_p \tag{3}$$

where each component contribution is determined from the projection of the component onto the peak wave direction θ_p:

$$\delta u_p = \delta u \cdot \left| \cos\left(\theta_p - \frac{\pi}{2}\right) \right| = \delta u \cdot \left| \sin\left(\theta_p\right) \right| \tag{4}$$

$$\delta v_p = \delta v \cdot \left| \cos\left(\theta_p\right) \right|. \tag{5}$$

The value $\pi/2$ was used for the projection in (4), as the positive direction of shear component δu was eastward (90° or $\pi/2$ radians relative to true N). A value of zero was used instead in (5), as the positive direction of component δv was northward. The absolute value of the cosine was used in (4) and (5) in order to provide the current shear projection onto the wave direction while also retaining the signs of the individual components. As discussed earlier, a negative current shear along the wave direction was expected to be an indicator of increased rogue wave likelihood. Here, a negative (positive) current shear in the direction of the waves will appear to the waves as negative (positive) regardless of whether the actual currents are directed with or against the waves. Note that, by this calculation, it is possible for a positive current shear in one component to partly or totally cancel out the effects of a negative current shear in the other component, depending on how they project onto the peak wave direction.
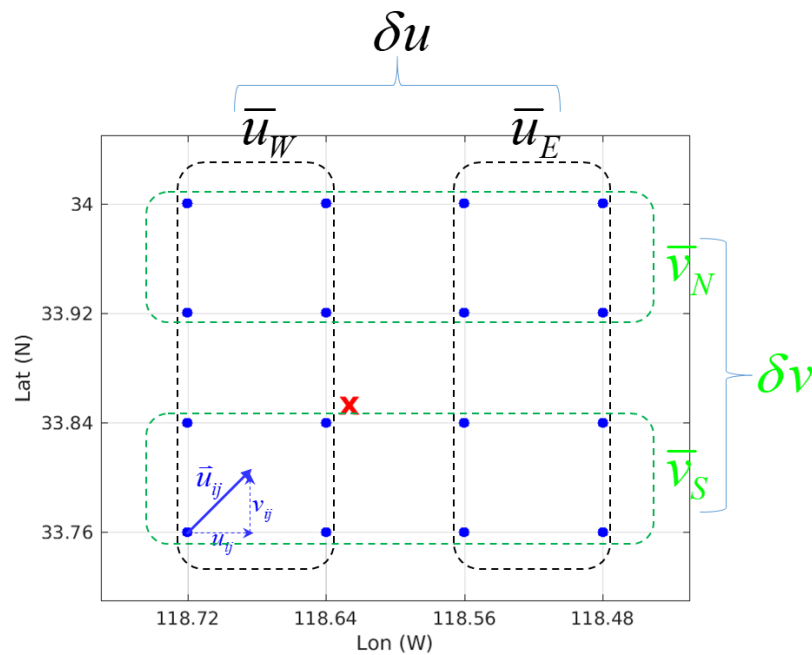
Figure 2. Determination of surface current shear, example for buoy 028 (located at red X). Velocity components $\bar{u}_E, \bar{u}_W, \bar{v}_N, \bar{v}_S$ are averaged from groups of 8 points to E, W, N, and S of buoy location, and then shear along each Cartesian axis ($\delta u, \delta v$) is determined from these averaged velocities.

Near surface (10 m) wind fields were obtained from the NCEP Climate Forecast System Reanalysis for the periods 1996–2010 (CFSRv1, ds093.1) and 2011–2019 (CFSRv2, ds094.1) at hourly intervals and 0.5° resolution [31,32]. The CFSR is a global coupled atmosphere–land–ocean–ice system with 64 atmospheric layers and 40 ocean layers. The reanalyses assimilate wind observations from satellite imagery, scatterometer, microwave imager data of the ocean surface, and numerous other sources. CFSR wind datasets are used in the generation of GOFS3.1 ocean surface currents and thus are the most appropriate choice for the present analysis.

Wind speed and direction are computed from the Cartesian components of the wind vectors (i.e., with U_w positive eastward and V_w positive northward):

$$\left|\vec{u}_w\right| = \sqrt{U_w^2 + V_w^2} \tag{6}$$

$$\theta_{\vec{u}_w} = atan2(V_w/U_w) \tag{7}$$

Equations (6) and (7) are used with the wind velocity components from the grid point nearest to each buoy location. The *atan2* function in Equation (7) returns four-quadrant inverse tangent values between $-\pi$ and π relative to east. Computed wind speeds have units of m/s and directions were converted to measure in degrees clockwise relative to true north (in nautical "from" convention).

Additional data were extracted for the full measurement period at each of the 34 buoys, including peak wave direction (nautical), peak period, significant wave height, and directional spread. The spectrum BFI was estimated (following [2] and [33]) as

$$BFI = \sqrt{2}\varepsilon/\delta_\omega \tag{8}$$

where $\varepsilon = k_p a$ is wave steepness, the product of peak wave number k_p and amplitude $a = H_s/2$, and $\delta_\omega = 1/(\sqrt{\pi}Q_p)$ is an estimate of frequency bandwidth based on peakedness factor Q_p [34].

For all times and locations in both the rogue and non-rogue datasets, this analysis compared the mean and maximum values of BFI and directional spread. We also examined the degree to which current shear and wind align either with or against the peak wave direction. As noted in Section 1,

negative surface current shear in the same plane as the wave direction has been shown to enhance wave nonlinearity in modeling and lab studies. As also described earlier, strong winds traveling in the primary wave direction were predicted to dampen nonlinearity and reduce the likelihood of rogue wave development in highly nonlinear seas, while winds opposing the peak waves may act to delay breaking and enable the continued growth of nonlinear instability. On this basis, we first examined overall mean wind and current statistics but then narrowed the focus of our analysis to include only times when large components of stronger current shear or winds are oriented either directly with or directly against the waves, seeking to identify a clear bias toward rogue event cases in comparison to non-rogue cases.

3. Results

Measured rogue wave heights averaged around 3–5 m at the 34 sites, with the largest waves at each site ranging from 4–25 m (Figure 3, top). Thirteen sites measured rogue waves with height exceeding 10 m. The mean ratio of H_r/H_s was only slightly above 2.0, but maximum values approached 3.0 (Figure 3, middle). Sites with the greatest ratios of H_r/H_s were primarily located along the California and Oregon coasts. Several sites had over 30 rogue waves recorded per year, while a similar number had fewer than 10 such events annually (Figure 3, bottom).
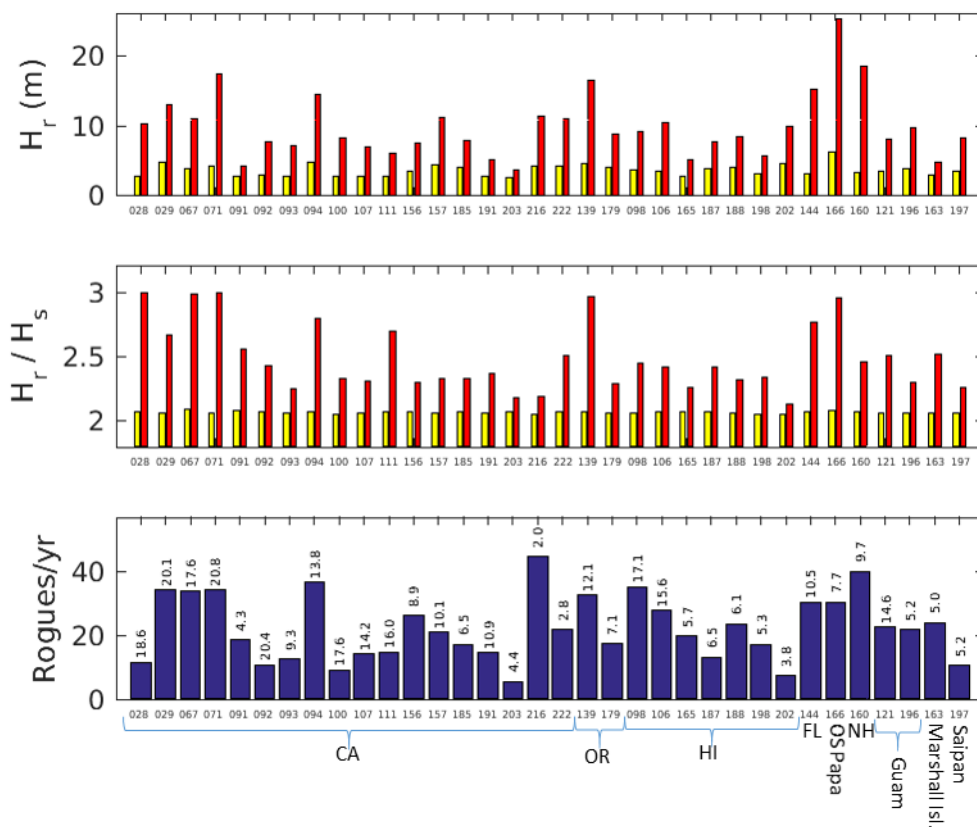
Figure 3. Rogue wave statistics at the 34 analyzed buoy locations. **Top panel**: Max (red bars) and Mean (yellow bars) rogue wave height. **Middle panel**: Max (red) and Mean (yellow) ratio of rogue height to significant wave height, as computed for each event at each buoy site. **Bottom panel**: Average number of rogues recorded per year at each site (values at top of each bar give total length of dataset at the site, in years). Buoy numbers are provided on the *x*-axis, with geographical buoy locations specified at bottom.

The results in Figure 3 were calculated using roughly 64 times as much data for non-rogue cases as for rogue cases, with buoy datasets of widely varying lengths (2–21 years). We would expect to have greater confidence in results for sites offering extensive datasets (e.g., buoy 029 with 20.1 yr.) than in those for sites with shorter datasets that may not be fully representative of longer term variations in climate (e.g., buoy 216 with 2.0 yr.). Some of the largest rogues were measured at Ocean Station Papa (buoy 166) in the Gulf of Alaska (e.g., Figure 4). Details of rogue wave event statistics are summarized in Table A2.
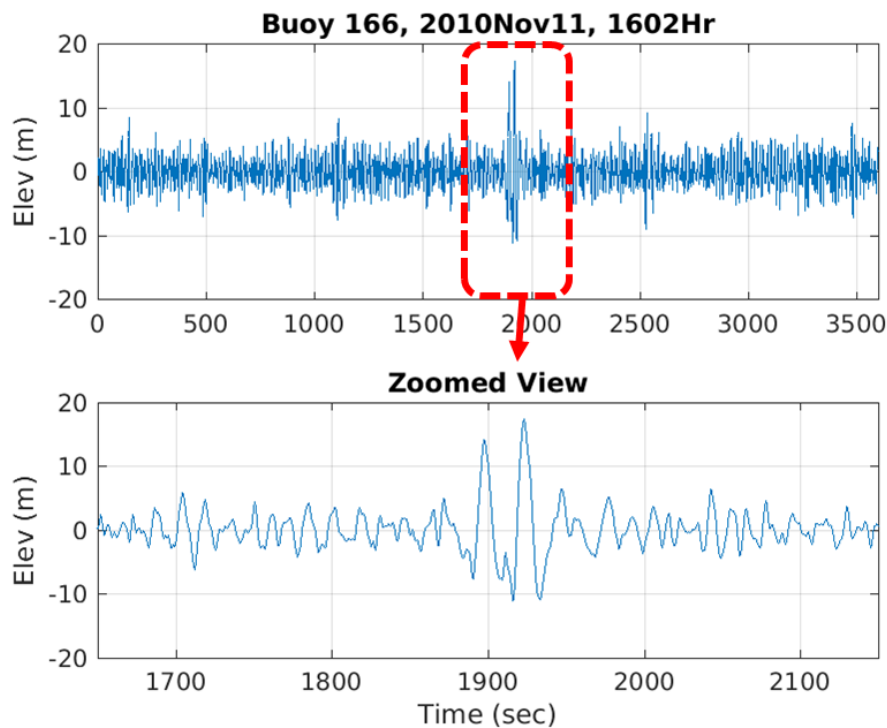
Figure 4. Top: Sample surface elevation time series from CDIP buoy 166, one hour of data beginning at 1602 UTC on Nov 11, 2010. Bottom: Zoomed view showing 500 s of data surrounding the 25.22 m rogue wave event. Ratio of H_r/H_s for the largest wave shown was 2.80.

Broadly averaged statistics of the wave spectral data at all times and locations in the rogue and non-rogue datasets suggested that both BFI and directional spread (i.e., σ_θ) provide some signaling that a rogue wave is more likely to occur (Table A3). As summarized in Figure 5, BFI values compiled from all identified rogue events tended to be larger than those obtained from the complete non-rogue dataset. The mean BFI value for the rogue wave data was 0.13, while the value averaged over the non-rogue data was 0.09. At nearly all individual buoy locations, the mean BFI corresponding to rogue events was found to be larger than that for the non-rogue cases, with mean BFI for rogue events exceeding that for non-rogue events by over 80% at six sites.
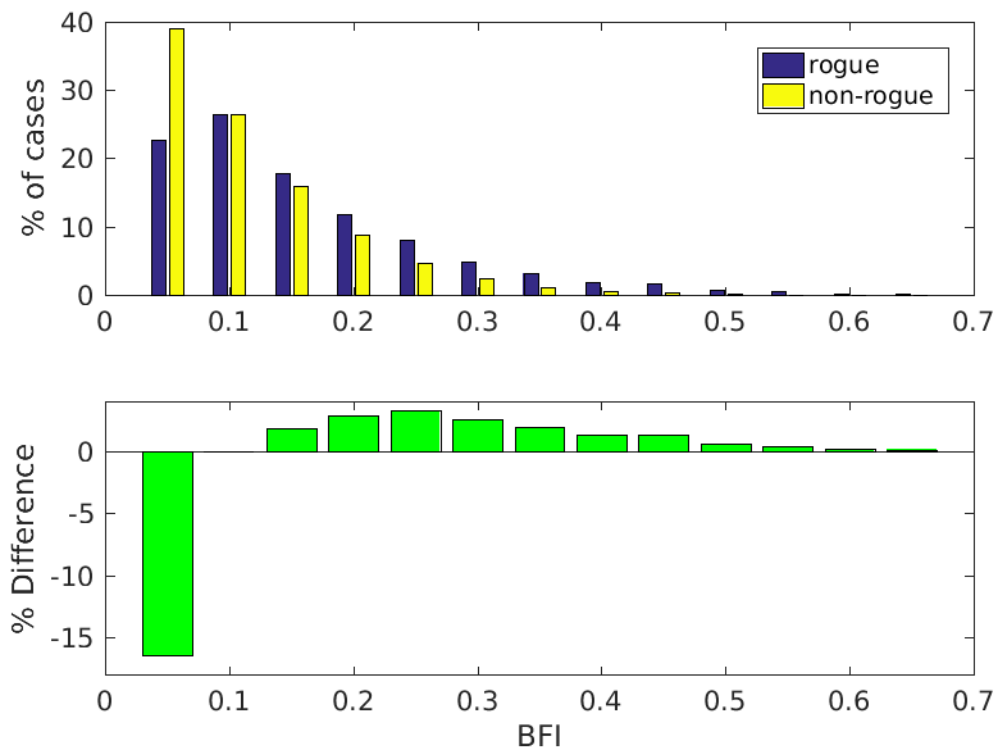
Figure 5. Comparison of BFI probability distributions for rogue and non-rogue datasets (all buoy locations combined). **Top panel**: Percentage of cases in selected BFI ranges for each dataset (bins centered from 0.05 to 0.65 with 0.05 width). **Bottom panel**: Difference in percentage of cases in selected BFI ranges. Positive values indicate a greater percentage of rogue wave events than non-rogue events for the specified BFI bin. (Values beyond 0.65 were too small to be visible on plots).

As has been noted by previous studies (e.g., [23]), the presence of the rogue wave itself in the time series can significantly affect the data statistics, in particular the higher moments used to compute kurtosis (κ) and the (related) value of BFI. To examine the extent to which individual rogue waves affected this and other results, we recomputed the parameters H_s, T_p, ε, κ, and BFI for each buoy rogue event dataset, comparing the statistics from the original data to the values when the rogue waves were removed and to the corresponding values from the non-rogue data (Figures 6 and 7, Table A4).

As anticipated, there were clear differences in rogue event statistics when rogue waves were excluded, particularly in values of kurtosis and BFI [35]. Other than a few exceptionally large wave heights with lower periods in the rogue data, the complete distributions of all H_s, T_p, and ε values for rogue event cases generally fit within the more broadly ranging distributions obtained for the much larger non-rogue dataset (Figure 6), providing some confirmation that the two datasets were extracted from the same general population. Mean values of these wave statistics included were only minimally affected (reduced by 1% or less) as a consequence of excluding individual rogue wave events (Table A4, rows 1–3). The average peak period for the rogue waves (~7.6 s) was noticeably smaller than the corresponding value for the non-rogue dataset (~11 s; Table A4, row 2), suggesting that rogue development may be more common in wind-forced seas than in conditions dominated by mature swell.
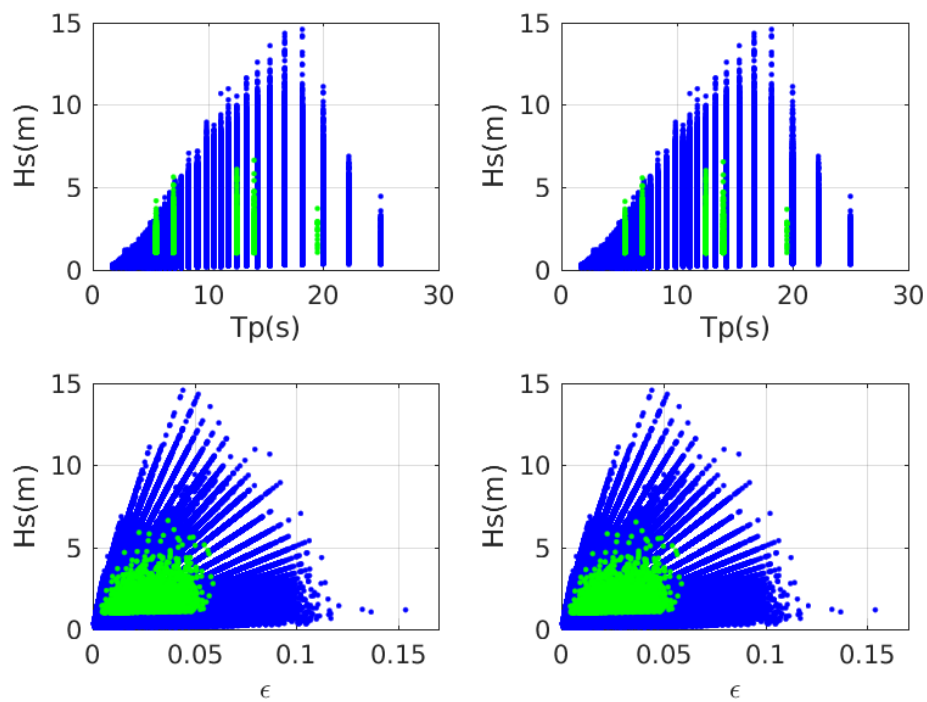
Figure 6. Comparison of H_s, T_p, and steepness (ε) distributions for rogue (green) and non-rogue (blue) datasets. Left panels have rogue statistics computed with rogue events included in each sample. Right panels have rogue statistics computed with rogue events excluded from each sample.
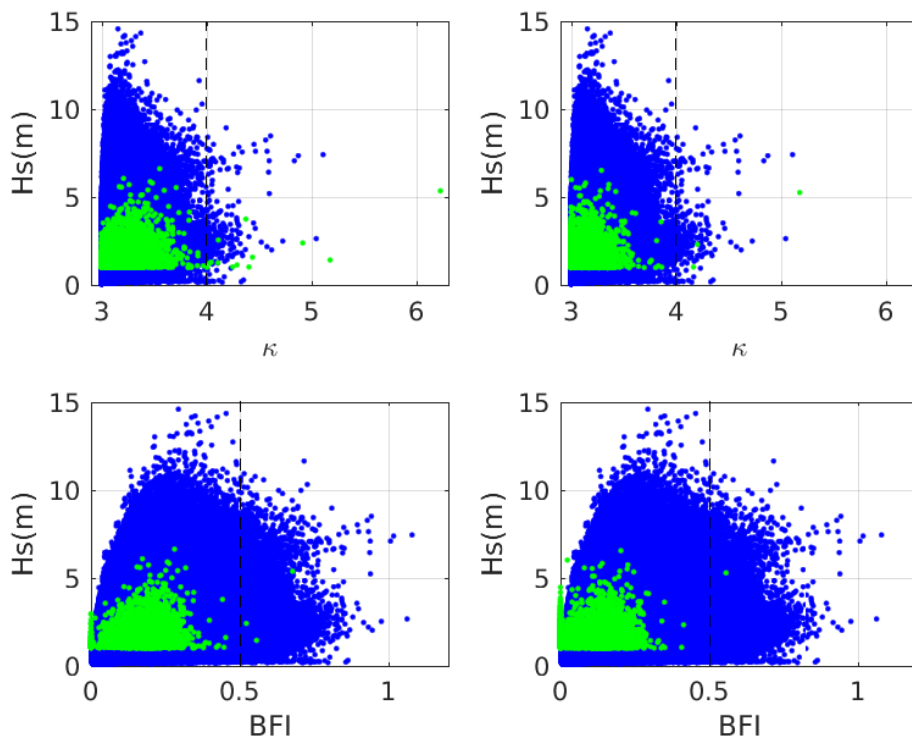
Figure 7. Comparison of H_s, kurtosis (κ), and BFI statistics for rogue (green) and non-rogue (blue) datasets. Left panels have rogue statistics computed with rogue events included in each sample. Right panels have rogue statistics computed with rogue events excluded from each sample. Heavier dashed vertical line added in each panel to better illustrate shift toward lower values when individual rogues are excluded.

While kurtosis and BFI distributions from the complete rogue dataset largely fit into the broader non-rogue ranges, there were a few exceptionally large κ and BFI values for H_s between 1 and 5 m and some very low values of BFI in the rogue data (Figure 7, left panels). Both κ and BFI were clearly affected by the exclusion of individual rogue events from the statistics calculations, with both distributions shifting leftward and most of the more extreme values disappearing (Figure 7, right panels). Mean kurtosis was reduced by 4% from 3.25 to 3.12 (Table A4, row 4). The BFI was most strongly affected by the exclusion of rogue events, with the mean value falling by 23% from 0.13 to 0.10 (Table A4, row 5). The reduced mean BFI for the rogue event dataset was still slightly larger than the value for the non-rogue dataset (0.09), but this small difference was likely not significant.

The mean directional spread of wave spectra in these data tended to be narrower for rogue wave cases than for non-rogue cases (Figure 8). Averaged over all cases, directional spread for rogue wave events was 25.0°, while for the non-rogue dataset, the value was 26.2°. The more general "factor space" over which the rogue wave percentages exceeded those of the non-rogue dataset is illustrated in Figure 9 by combining the BFI and σ_θ results into a 3D difference histogram plotted for the BFI-σ_θ plane, with values that are a function of both factors. Summing along either axis results in the two-dimensional (2D) difference histogram of Figure 5 or 8, and the entire 3D histogram sums to zero.
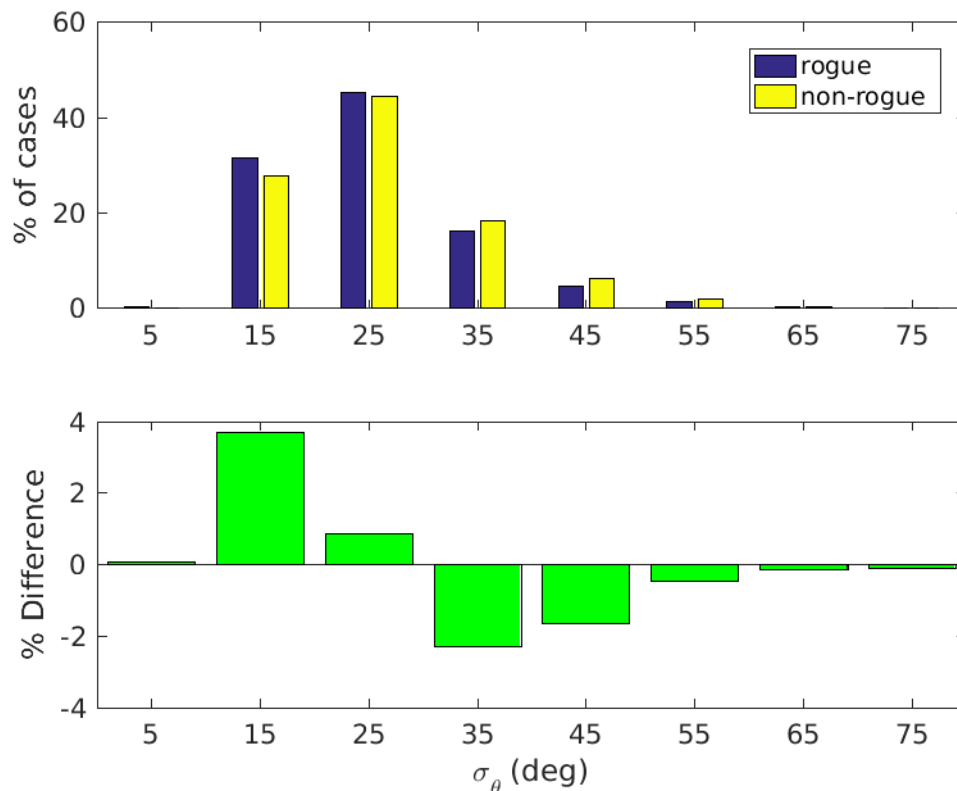
Figure 8. Comparison of directional spread (σ_θ) probability distributions for rogue and non-rogue datasets (all buoy locations combined). **Top panel**: Percentage of σ_θ cases in selected angle ranges for each dataset (bins centered from 5° to 75° with 10° width). **Bottom panel**: Difference in percentage of cases in same directional spread bins. Positive values indicate a greater percentage of rogue wave events than non-rogue events for the specified bin.
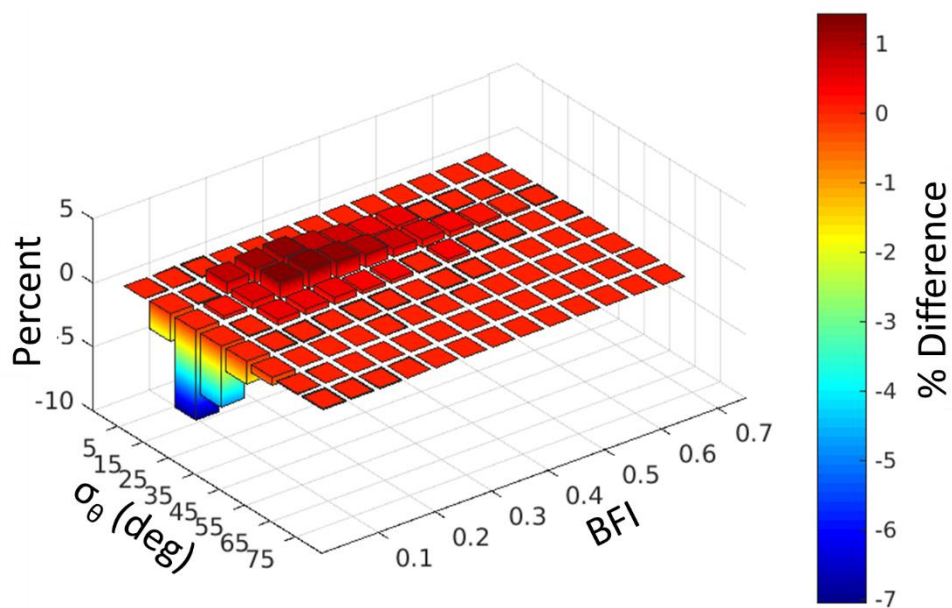
Figure 9. Combined difference histogram showing percentage difference (rogue minus non-rogue) as a function of both BFI and directional spread (σ_θ), all buoy locations combined.

Among individual buoy sites, results were somewhat more uneven than those for BFI, but they still tended to support theoretical predictions of narrower spreading for rogue wave spectra (Figure 10). Mean directional spread varied from 17.7° to 38.7° for rogue events versus 19.0°–41.8° for non-rogue cases. The value of $\overline{\sigma_\theta}$ for non-rogue data exceeded that for rogue data, at 26 of 34 locations, by up to 8.1° (29%), while at the remaining 8 sites, $\overline{\sigma_\theta}$ for rogue events was generally less than 1° (5%) above the non-rogue value.
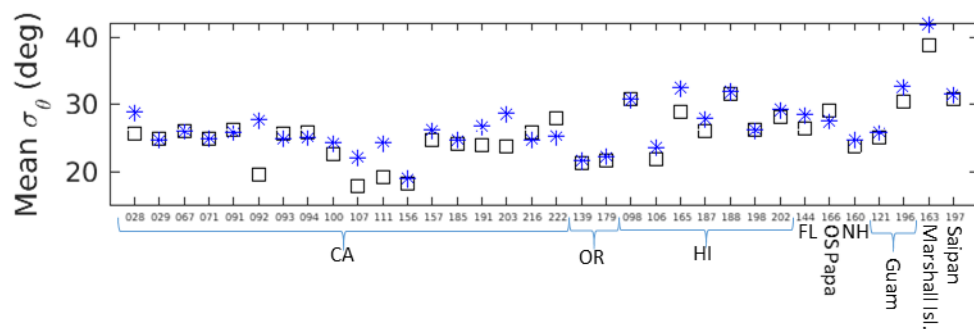
Figure 10. Average directional spread for rogue and non-rogue cases at all analyzed buoy sites. X-axis labels indicate buoy number and location. Rogue event data are depicted by black squares, and non-rogue data are shown as blue asterisks.

The greatest directional spreads were seen at the Marshall Islands site (buoy 163) in the southwestern Pacific Ocean. Mean values over 30° were also found at sites near Guam, Hawaii, and Saipan, likely a consequence of the unbounded nature of these sites, but possibly also occasionally due to effects of wave refraction around the nearby islands.

At four sites (buoys 092, 107, 111, and 156), the mean directional spread values for the rogue event dataset were less than 20°. For the first three of these sites, the mean spread for rogue events was much narrower than that for the non-rogue dataset, suggesting that local conditions affecting wave direction may have played a more important role in fostering rogue wave development at these sites. All four sites are moored in sheltered locations off of California, with three (092, 107, 111) toward the southern end and one (156) in outer Monterey Bay along the central coast. The three southern buoys

are each located in channels between the coastline and offshore islands (Anacapa Passage and San Pedro Channel), while the central coast buoy is partially sheltered by the edges of the bay to the north and south. The time series of wave direction and directional spread at each location had clear seasonal patterns, with narrower spreads and waves primarily from the north/northwest in winter months (i.e., Dec–Feb) but much broader directional variability at other times of year. For example, the mean directional spread for the full dataset at buoy 092 was 23° in winter versus 29° over the remaining nine months. Rogue wave events at each of the southern sites also tended to be more common during the same three winter months, making up 31%, 38%, and 44% of identified rogue waves at buoys 111, 107, and 092, respectively. In contrast, winter rogue wave events at buoy 156 made up only 25% of total recorded events. These results suggest that wave refraction and blocking by the offshore islands acted to reduce rogue wave likelihood during non-winter months, increasing the spread of the more southerly incoming waves and also blocking some of their overall energy (though it has not been confirmed that rogue waves are less likely under low-energy conditions).

The overall statistics for negative current shear in this study initially showed just a weak correlation with rogue wave events. As noted in Section 1, it was expected that rogue wave development would be more likely when the wave direction was aligned either with or against currents that have a negative shear. In this analysis, we found that negative current shear of any kind (i.e., $\delta u < 0$ or $\delta v < 0$) occurred equally often (81.4%) in the rogue and non-rogue data. There was just a slightly greater percentage of negative shear aligned with the wave direction (i.e., $\delta U_p < 0$) and a slightly larger mean shear ($\overline{\delta U_p}$) for rogue wave cases than for non-rogue data (Table A3). At most buoy sites in this study, the mean current shear projected onto the peak wave direction was similar for rogue and non-rogue cases (Figure 11). Of the 34 sites, thirteen had negative mean shear for both datasets.
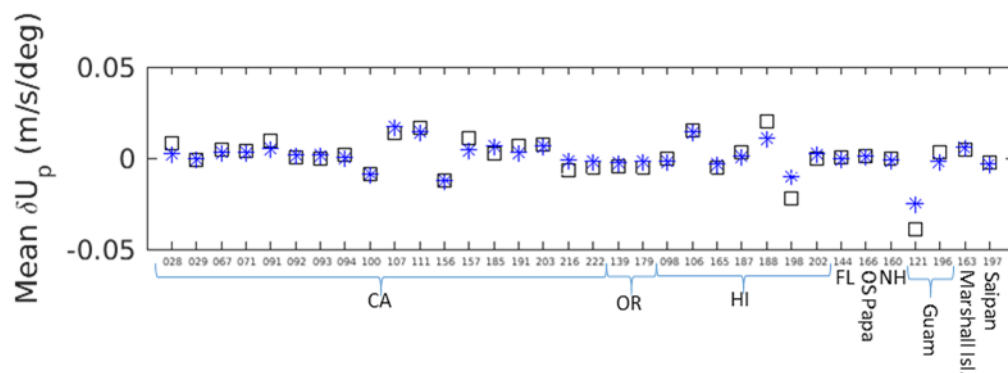
Figure 11. Average of current shear acting along the line of the peak wave direction, at all analyzed buoy sites. X-axis labels indicate buoy number and location. Rogue event data are depicted by black squares, and non-rogue data are shown as blue asterisks.

When we restricted the current data to more idealized, quasi-2D conditions in which a stronger negative current shear component was aligned with the peak wave direction, we found additional evidence of a causal relationship for specific cases. Limiting the rogue and non-rogue datasets to only those cases where $\delta U_p < -0.50$ m/s/°, we found that the rogue event data contained 17% more of such conditions, proportionally, than did the non-rogue dataset. When the datasets were further limited to cases with narrower wave directional spread ($\sigma_\theta < 20°$), the rogue wave records were found to have a nearly 50% greater rate of occurrence of such states than the non-rogue data.

Notably, the two sites in Figure 11 with the largest negative mean current shear (buoys 198 and 121) also featured the largest difference between the rogue and non-rogue results, with the magnitude of the shear in the rogue event data exceeding that in the non-rogue data by 125% and 60%, respectively. The results suggest that there may be a critical "threshold" value for negative current shear magnitude at which the modulating effects of such shear on the wave spectrum become clearly measurable. Buoy 198 is located off of Kāne'ohe Bay, HI, to the east of O'ahu in a region of significant surface current

vorticity, where the island blocks the generally westward-flowing currents of the North Pacific Gyre. Buoy 121 is moored along the southeast coast of Guam, also in a region of higher vorticity; in this case, the island's coastline acts as a barrier to the northwestward-flowing North Equatorial current. Both buoys are in intermediate depth, suggesting that interactions with the seabed may also have some effects on shoaling of longer waves. Few if any of the other 32 sites share these specific features. This provides solid (albeit site-specific) support for the theoretically predicted greater correlation of negative current shear with rogue events, hinting that the shear threshold may be reached more often at sites with greater surface current vorticity (and possibly intermediate water depths).

Overall statistical averages for wind forcing also initially provided just limited support for a causal connection with rogue wave development. Mean wind magnitudes for the rogue event and non-rogue datasets ranged from 2 m/s to over 10 m/s, and the relative directions of wind and waves varied widely among the locations (Figures 12 and 13). At most sites, the wind direction was within 45° of the wave direction (red dashed lines in Figure 13), suggesting that the wave environment at the majority of locations was dominated by wind seas. Mean results for the complete datasets were very similar for rogue event and non-rogue cases (Table A3). For these results to generally support the predictions of [1] and [13], and Simeonov et al. discussed in Section 1, it would be expected that the rogue event data would have a smaller percentage of strong co-directed winds (which dampen rogue wave development) and a greater percentage of opposing winds (which enhance rogue wave development), in comparison to the non-rogue dataset.
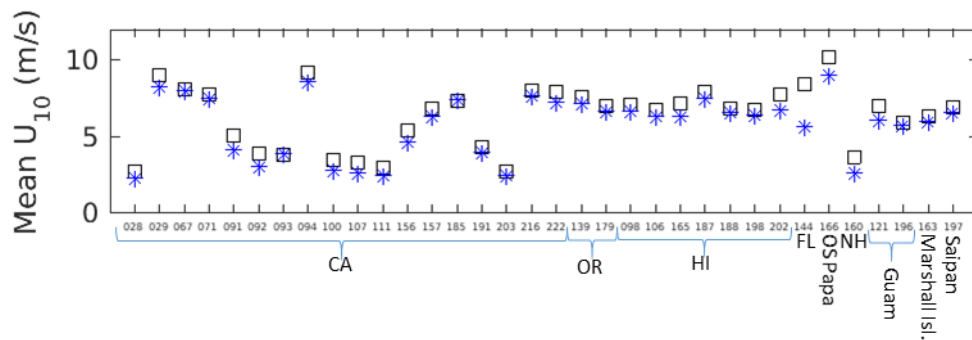
Figure 12. Average wind magnitude at each buoy location for rogue event and non-rogue cases. Rogue event data are depicted by black squares, and non-rogue data are shown as blue asterisks.
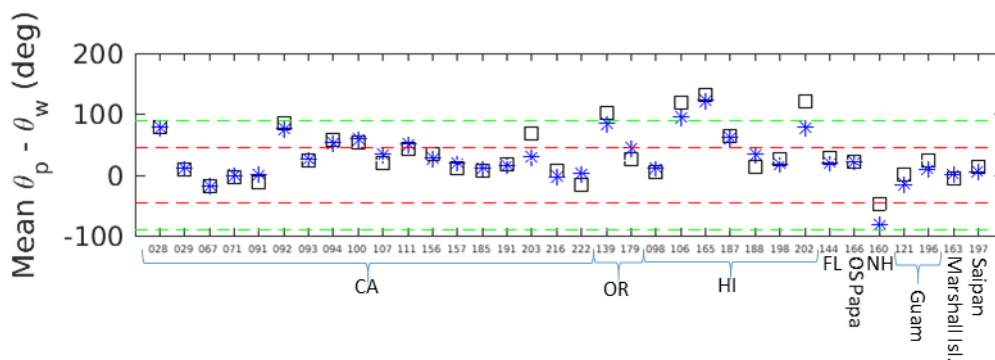
Figure 13. Average differences between wave peak direction (θ_p) and wind direction (θ_w) for rogue event and non-rogue cases. Rogue event data are depicted by black squares, and non-rogue data are shown as blue asterisks. Red dashed lines mark ±45°. Green dashed lines mark ±90°.

Overall, nearly 90% of both the rogue and non-rogue datasets consisted of cases where the wind had some component from the same direction as the waves. When the complete datasets were restricted to cases with moderately strong winds ($U_{10} > 10$ m/s) from nearly the same direction as the peak waves (±20°), the remaining cases accounted for 9.5% of the rogue wave dataset, while they comprised just

6.3% of the non-rogue data. If the rogue wave development were damped by the wind, it would seem reasonable to expect proportionally fewer rogue event cases with stronger co-directed winds, but this was not seen here.

If we instead examine these datasets under the specific and extreme wind magnitude criteria suggested by the theoretical analyses, however, evidence emerges that may support the hypothesized wave damping by co-directed winds. As noted in Section 1, results from [1] and [13] suggested that co-directed wind magnitudes need to be quite large—with U_{10} exceeding either 33 m/s or four times the wave phase speed—in order to significantly dampen nonlinear growth. For typical waves with peak period of at least 10 s, the latter criterion would require a minimum wind speed of over 60 m/s (well beyond hurricane strength!). Reviewing all event times and locations in the complete rogue wave dataset, we found that the maximum estimated value of U_{10} for any event was 22.95 m/s. In contrast, the maximum winds in the non-rogue dataset reached 38.4 m/s, with over 80 non-rogue cases of wind magnitudes exceeding the maximum U_{10} value for rogue events. In four of these cases, the wind speeds reached hurricane strength. This result implicitly suggests that rogue waves may have been prevented from developing during some episodes of extreme winds with U_{10} approaching the levels predicted by [1] and [13].

We find that the average winds in the two datasets opposed the waves to some degree (i.e., absolute direction difference $\left|\theta_p - \theta_w\right| > 90°$, marked by green dashed lines in Figure 13) at just 4 of the 34 buoy sites analyzed for rogue event data (buoys 106, 139, 165, and 202). The same four sites also had opposing average winds in the non-rogue data. Two of these sites (106, 139) had higher than the overall average of rogues per year, while the other two had lower than that average. The site with the most nearly opposing winds (Hawaii, buoy 165, with relative angle of 131°) saw about 19 rogues/yr., while the site with the second most opposing winds (buoy 202, relative angle of 122°) usually received only 6 rogues/yr. There was no clear evidence of a stronger correlation with rogue waves in the averaged data.

Once again, however, the comparisons for this causal factor were somewhat more in agreement with theoretical predictions for conditions closer to an idealized, quasi-2D scenario. When the complete datasets were restricted to only cases with moderately strong winds (i.e., $U_{10} > 10$ m/s) from nearly opposite to the wave direction (i.e., opposition ±20°), we found that such conditions were more than twice as likely to be associated with rogue event data as with non-rogue cases (i.e., 1.1% vs. 0.4% of all cases, respectively). These results suggest that directly opposing winds may facilitate the development of rogue waves in some cases by postponing the breaking of the steepening wave fronts, in essentially the same manner as offshore winds at the coastline can delay the breaking of nearshore waves and allow surfers a longer ride [36].

4. Discussion and Conclusions

To date, nearly all analyses indicating significant correlations between rogue wave events and specific environmental factors have come from theoretical, modeling, or lab-based studies. Few attempts have been made to investigate these relationships in the open ocean, where conditions are far more complex and uncontrolled. The present effort utilizes an extensive dataset of measured rogue wave events in combination with current and wind data from state-of-the-art global coupled models, under the assumption that correlations should be measurable to some degree in such a large dataset if they do indeed exist. While the spectra and statistics for CDIP buoys are generally computed using approximately 20 min of data (i.e., 1600 points at 1.28 Hz), we chose here to use hour-long sections of the buoy positional time series for identification of rogue events. A 20-min data section will contain roughly 100 "typical" waves ($T \sim 8$–10 s), implying that H_s will be determined from the mean of around 30 largest waves. Using hour-length sections allowed us to compute H_s from roughly 100 waves, a more robust estimate less likely to be strongly influenced by outliers. As both the rogue and non-rogue datasets were processed with the same one-hour record length, ergodicity/stationarity effects impacted both rogue and non-rogue datasets in the same way and did not alter the statistical

differences computed between them (though this approach may cause issues when comparing these results to those from other studies based on 20-min samples).

This investigation provides support for the role of nonlinear frequency modulation, wave directional spread, surface current shear, and wind forcing in increasing the likelihood of rogue wave development. We demonstrate that the BFI distribution for the rogue event dataset is significantly shifted toward larger values in comparison with the distribution for non-rogue data, and we find that the mean BFI for rogue events is 45% greater than for non-rogue cases. Removing the individual rogue waves from each analyzed sample in the rogue event dataset reduces mean BFI by 23%, to a value that is only slightly larger than the average BFI for the non-rogue dataset, suggesting that nonlinear modulation played only a limited role in the rogue wave development. A comparison of directional spread distributions of rogue wave and non-rogue wave datasets shows that rogue waves have a higher probability of narrower directional spreading. Mean directional spread of rogue wave events is about 5% narrower than non-rogue cases. We also find evidence at several sites that directional spreads can be seasonally narrowed in channels and passages created by offshore islands, potentially contributing to increased rogue wave likelihood in such locations at specific times of year.

When overall statistical averages are compared, horizontal current shear shows only slightly greater correlations for rogue wave events than for non-rogue data. However, when these data are examined at the individual sites (Figure 11), we find at least two locations at which rogue wave events correlate with significantly stronger negative current shear. These locations also have the highest mean shear magnitudes of all sites, suggesting that a specific threshold negative shear may need to be exceeded before the effects can be detected. While this study does not derive a universal rule for the wave-modulating effects of surface current shear, the results do suggest that larger negative shear along with other environmental conditions at specific sites, such as high surface current vorticity and/or intermediate water depth, may provide useful indicators of potential rogue wave events.

Like the current shear, average wind forcing data also show only slightly greater correlations for rogue wave events than for non-rogue data. However, when these cases are restricted to those with stronger forcing, a clear difference emerges in the wind datasets. Intense wind conditions (i.e., $U_{10} > 23$ m/s) do not occur during any of the 8013 recorded rogue wave events, while in contrast there are over 80 occurrences of such gale- and hurricane-force winds in the non-rogue dataset, suggesting that these stronger winds may have prevented rogue development when they did occur. In addition, opposing winds of moderate strength (i.e., $U_{10} > 10$ m/s) were found to be twice as strongly associated with rogue wave events as with non-rogue data.

Using a standard Rayleigh distribution of wave heights with significant wave height H_s, the likelihood of occurrence of a rogue wave following the standard definition (i.e., $H_r > 2H_s$) is approximately 0.03% (i.e., 3 in 10,000). Here, 8013 rogue waves are identified from a combined dataset of approximately 800 million individual waves, which nominally corresponds to an occurrence rate of about 0.001%, well under the Rayleigh-predicted rate. However, surface-following wave buoys tend to underestimate wave heights of larger and steeper waves [23], making it likely that this tally is somewhat less than the actual total. In such cases, buoys tend either to get dragged through the crest or slide down the side of the main crest peak. Because buoys offer only point measurements, there is also a relatively small chance that a given rogue developing in the vicinity of a buoy will pass directly over that buoy. While the buoy may provide a reasonable estimate of overall conditions using a 1 h time series, it may only capture, say, the fourth or fifth highest wave that passes within a few-hundred-meter radius of the buoy over that hour.

The strict selection methods of this analysis likely also excluded a number of measured rogue waves, such as those occurring in so-called "three-sisters" formations (from which only one rogue would have been selected). In addition, observations may have had a seasonal bias if some months were over-represented. For example, buoys tended to go offline or have their moorings broken more often in winter months with larger waves. This likely contributed to an overemphasis in the overall dataset of smaller rogue waves that occurred during less extreme periods. These conclusions are also

supported by the results presented in Figure 7, in which the rogue dataset contains very few confirmed events with more extreme values of kurtosis or BFI in comparison to the non-rogue data. This suggests that an even more extensive buoy dataset than ours may be required to fully capture the distribution of rogue waves in the oceans. It also provides support for a primary motivating hypothesis of this study—that rogue wave prediction cannot be based solely on wave statistics but must also include other external environmental factors like currents and wind.

Our comparison analyses might be improved if better representations of the actual ocean and atmospheric states from model data were available, with higher spatial and temporal resolutions. The horizontal resolution of HYCOM surface current data (~8 km) used in this study was not fine enough to properly represent submesoscale eddies, whose horizontal surface shear could potentially have had more intense localized effects on steepening individual nonlinear wave peaks than those that we estimated from the larger-scale surface shear. CFSR wind data resolution (~50 km) did not capture microscale atmospheric features such as near-surface turbulence and localized gusts, either of which could in principal act on individual waves to either dampen or sustain their growth. Both the surface current and the wind data were provided at 6-h intervals, requiring this analysis to assume stationary ocean and atmospheric conditions for periods up to several hours. In addition, the HYCOM and the CFSR model systems, while relatively accurate on the global scale, still contain significant error at local levels. For example, HYCOM currents were found to have an RMS error of 0.35 m/s in magnitude and 43° in direction in a study of the Agulhas region [37], while RMS errors for CFSR winds have been estimated at around 3 m/s for magnitude [38] and 28° for direction [39]. These uncertainties highlight the present limitations of a field-based validation of rogue wave causal factors.

Alternative data sources may also ultimately help to improve these analyses by extending them to more diverse open ocean locations around the world. The data in this study are primarily from buoys moored in U.S. coastal waters. A fleet of over 200 GPS-equipped surface buoys was recently deployed in the Pacific Ocean by the San Francisco-based company Sofar (https://www.sofar.com), featuring near-real-time monitoring of conditions as well as surface elevation time series and thus more than doubling the number of measurement locations that have been available from CDIP. Satellite-derived current and wind data are also becoming increasingly available and accurate, helping to improve the performance of global circulation models and perhaps eventually even replacing them in analyses such as this one.

Effects of water depth on rogue wave development were not explicitly examined in this analysis (although water depth effects on wave steepness and rogue wave development are implicitly included in the BFI). A scatter plot of buoy depth versus rogues/yr. at the 34 sites shows essentially no correlation between depth and rogue occurrences (Figure 14), indicating that shoaling effects did not by themselves strongly influence the likelihood of rogue waves. However, this analysis suggests that the seabed may affect individual causal factors when combined with other site-specific conditions. As noted above, we detected larger than average negative surface current shear at two Pacific island sites (buoys 198 and 121) that were in relatively shallower depths (81 m and 200 m, respectively). The shear seemed primarily due to vorticity generated by the islands' blocking effects on larger ocean circulation patterns, but it may also have been augmented in the shallower regions.
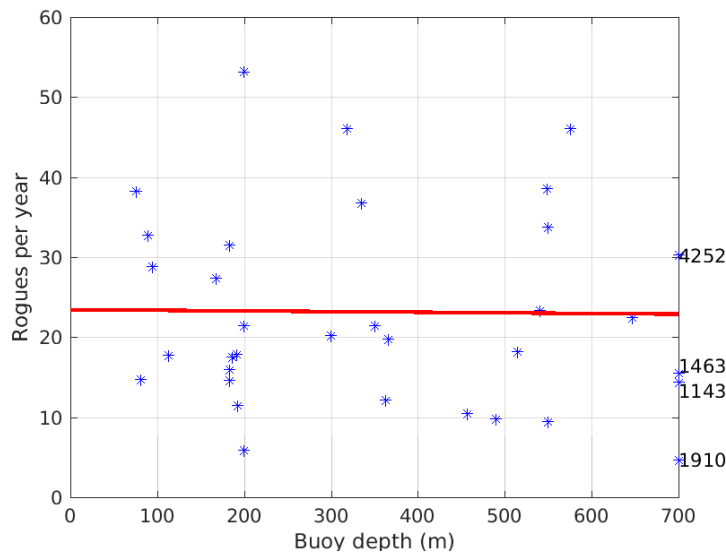
Figure 14. Rogue events per year versus water depth at each of the 34 buoy locations. Individual values plotted as blue asterisks, with best-fit shown by red line. Locations with depth greater than 700 m are plotted along the right vertical axis, with depth values listed next to each asterisk.

Appendix A. Tabulated Results

This appendix provides more detailed results from our analysis of rogue wave events and associated causal factors.

Table A1. Buoy data analyzed for this study.

Buoy #	Location and Depth [1]	Time Range	Length (Years) [2]
028	CA: 118.6W, 33.8N, 363 m	4/00–12/18	18.6
029	CA: 123.5W, 37.95N, 550 m	12/96–12/18	20.1
067	CA: 119.9W, 33.2N, 335 m	1/00–12/18	17.6
071	CA: 120.8W, 34.45N, 549 m	3/98–12/18	20.8
091	CA: 117.4W, 32.6N, 186 m	12/95–8/05	4.3
092	CA: 118.3W, 33.6N, 457 m	3/98–12/18	20.4
093	CA: 117.4W 32.75N, 192 m	11/97–12/15	9.3
094	CA: 124.7W, 40.3N, 319 m	4/99–12/18	13.8
100	CA: 117.4W, 32.9N, 550 m	2/01–12/18	17.6

Table A1. *Cont.*

Buoy #	Location and Depth [1]	Time Range	Length (Years) [2]
107	CA: 119.8W, 34.3N, 183 m	7/02–8/16	14.2
111	CA: 119.4W, 34.2N, 113 m	7/02–12/18	16.0
156	CA: 121.95W, 36.8N, 168 m	6/07–5/16	8.9
157	CA: 122.1W, 36.3N, 366 m	11/08–12/18	10.1
185	CA: 122.35W, 36.7N, 1463 m	10/11–12/18	6.5
191	CA: 117.4W, 32.5N, 1143 m	10/07–12/18	10.9
203	CA: 119.6W, 33.8N, 1910 m	7/13–12/18	4.4
216	CA: 120.8W, 34.4N, 576 m	7/15–12/18	2.0
222	CA: 121.5W, 34.8N, 647 m	3/16–12/18	2.8
139	OR: 124.55W, 43.8N, 183 m	8/06–12/18	12.1
179	OR: 124.6W, 46.1N, 183 m	4/11–12/18	7.1
098	HI: 157.7W, 21.4N, 89 m	8/00–12/18	17.1
106	HI: 158.1W, 21.7N, 200 m	1/02–12/18	15.6
165	HI: 158.1W, 21.2N, 300 m	11/10–12/17	5.7
187	HI: 156.4W, 21.0N, 193 m	12/11–12/18	6.5
188	HI: 155.0W, 19.8N, 350 m	3/12–12/18	6.1
198	HI: 157.75W, 21.5N, 81 m	11/12–12/18	5.3
202	HI: 159.6W, 22.3N, 200 m	10/13–12/18	3.8
144	FL: 84.3W, 27.3N, 94 m	7/07–12/18	10.5
166	Oc. Stn. Papa: 145.2W, 50.0N, 4252 m	7/10–12/18	7.7
160	NH: 70.2W, 42.8N, 76 m	9/08–12/18	9.7
121	Guam: 144.8E, 13.35N, 200 m	8/03–12/18	14.6
196	Guam: 144.8E, 13.7N, 515 m	11/12–12/18	5.2
163	Marshall Isl.: 171.4E, 7.1N, 540 m	5/16–12/18	5.0
197	Saipan: 145.7E, 15.3N, 490 m	11/12–12/18	5.2

[1] CA = California coast; HI = Hawaii region; OR = Oregon coast; FL = Florida coast; NH = New Hampshire coast; Location given as Lon (deg), Lat (deg), Depth (m). [2] Length analyzed excludes data gaps.

Table A2. Rogue wave event summary.

Buoy #	Location	Rogues per Year	H_r (m) Mean	H_r (m) Max	H_r/H_s Mean	H_r/H_s Max	Number of Rogue Events Total	$H_r > 6$ m	$H_r > 10$ m
028	CA	11.51	2.69	10.18	2.07	2.99	214	1	1
029	CA	34.13	4.66	12.99	2.06	2.67	686	143	6
067	CA	33.75	3.89	10.84	2.09	2.98	594	51	2
071	CA	34.04	4.11	17.34	2.06	2.99	708	84	5
091	CA	18.60	2.61	4.24	2.07	2.55	80	0	0
092	CA	10.69	2.81	7.61	2.07	2.42	218	5	0
093	CA	12.47	2.79	7.13	2.06	2.24	116	2	0
094	CA	36.52	4.71	14.41	2.07	2.79	504	119	12
100	CA	9.09	2.74	8.24	2.05	2.33	160	2	0
107	CA	14.01	2.75	6.95	2.06	2.31	199	1	0
111	CA	14.75	2.79	5.96	2.07	2.69	236	0	0
156	CA	26.18	3.41	7.40	2.06	2.30	233	6	0
157	CA	20.89	4.42	11.14	2.06	2.33	211	29	5
185	CA	17.08	3.98	7.80	2.06	2.33	111	12	0
191	CA	14.50	2.72	5.08	2.06	2.37	158	0	0
203	CA	5.45	2.57	3.58	2.07	2.18	24	0	0
216	CA	44.50	4.23	11.23	2.05	2.18	89	14	1
222	CA	21.79	4.19	10.92	2.06	2.50	61	7	1
139	OR	32.56	4.54	16.34	2.07	2.96	394	73	13
179	OR	17.32	4.00	8.81	2.05	2.29	123	16	0
098	HI	35.09	3.61	9.02	2.06	2.45	600	12	0
106	HI	27.63	3.47	10.38	2.07	2.41	431	21	1

Table A2. *Cont.*

Buoy #	Location	Rogues per Year	H$_r$ (m) Mean	H$_r$ (m) Max	H$_r$/H$_s$ Mean	H$_r$/H$_s$ Max	Number of Rogue Events Total	Number of Rogue Events H$_r$ > 6 m	Number of Rogue Events H$_r$ > 10 m
165	HI	19.65	2.74	5.14	2.06	2.26	112	0	0
187	HI	13.08	3.81	7.56	2.06	2.41	85	6	0
188	HI	23.44	4.04	8.39	2.06	2.32	143	12	0
198	HI	17.17	3.15	5.70	2.04	2.33	91	0	0
202	HI	7.37	4.50	9.87	2.05	2.13	28	4	0
144	FL	30.38	3.08	15.19	2.06	2.76	319	13	1
166	OS Papa	30.26	6.20	25.22	2.08	2.95	233	91	22
160	NH	40.00	3.30	18.42	2.07	2.46	388	18	4
121	Guam	22.60	3.40	8.05	2.06	2.50	330	8	0
196	Guam	21.73	3.71	9.65	2.06	2.30	113	6	0
163	Marsh. Is.	24.00	2.88	4.63	2.06	2.51	120	0	0
197	Saipan	10.58	3.48	8.19	2.05	2.26	55	1	0
ALL	–	22.54	3.77	25.22	2.07	2.99	8013	731	71

Table A3. Summary of overall statistical analysis.

Parameters	Rogue Wave	Non-Rogue Wave	Δ (%) [1]
Max BFI	0.70	1.09	–0.49 (–57.1%)
Mean BFI	0.13	0.09	0.04 (46.6%)
Mean directional spreading $\bar{\sigma}_\theta$	25.0	26.2	–1.2 (–4.4%)
Probability of $\delta_u < 0$ or $\delta_v < 0$, %	81.4	81.4	0.0
Probability of $\delta U_p < 0$, %	47.8	47.5	0.3
$\delta \bar{U}_p$, m/s/deg	0.037	0.035	0.002 (5.7%)
Mean wind speed $\bar{U}_{10}$ (m/s)	6.8	5.5	1.3 (23.6%)
Mean direction difference $\theta_p - \theta_w$, deg	78.9	87.3	-

[1] Δ is rogue waves minus non-rogue waves. % is difference divided by smaller value in each case.

Table A4. Averages of wave statistics for rogue dataset, computed with identified rogues included/excluded, compared to mean values from non-rogue dataset.

	Rogue Means Include	Rogue Means Exclude	% Diff	Non-Rogue Means
H_s	1.76	1.75	0.77%	1.75
T_p	7.61	7.57	0.45%	11.12
ε	0.027	0.027	0.54%	0.018
κ	3.25	3.12	4.0%	3.03
BFI	0.13	0.10	23.0%	0.09

References

1. Babanin, A.; Rogers, W.E. Generation and limiters of rogue waves. *Int. J. Ocean Clim. Syst.* **2014**, *5*, 39–49. [CrossRef]
2. Janssen, P.A.E.M. Nonlinear four-wave interactions and freak waves. *J. Phys. Oceanogr.* **2003**, *33*, 863–888. [CrossRef]
3. Baschek, B.; Imai, J. Rogue wave observations off the US West Coast. *Oceanography* **2011**, *24*, 158–165. [CrossRef]
4. Orzech, M.; Simeonov, J.; Manolidis, M. *Development and Testing of a Rogue Wave Threat Estimator for WAVEWATCH III®*; US Naval Research Laboratory: Louisiana, MS, USA, 2019.
5. Kharif, C.; Pelinovsky, E. Physical mechanisms of the rogue wave phenomenon. *Eur. J. Mech. B Fluids* **2003**, *22*, 603–634. [CrossRef]

6. Toffoli, A.; Onorato, M.; Cavaleri, L.; Gramstad, O.; Janssen, P.; Monbaliu, J.; Osborne, A.; Serio, M.; Stansberg, C.; Trulsen, K. Statistical properties of mechanically generated surface gravity waves: A laboratory experiment in a 3D wave basin. *J. Fluid Mech.* **2009**, *627*, 235–257.

7. Waseda, T.; Kinoshita, T.; Tamura, H. Evolution of a random directional wave and freak wave occurrence. *J. Phys. Oceanogr.* **2009**, *39*, 621–639. [CrossRef]

8. Manolidis, M.; Orzech, M.; Simeonov, J. Rogue wave formation in adverse current gradients. *J. Mar. Sci. Energy* **2019**, *7*. [CrossRef]

9. Onorato, M.; Proment, D.; Toffoli, A. Triggering rogue waves in opposing currents. *Phys. Rev. Lett.* **2011**, *107*, 184502. [CrossRef]

10. Orzech, M.; Wang, D. *Rogue Wave Events in Time Series of Surface Elevation*; US Naval Research Laboratory: Louisiana, MS, USA, 2019.

11. Babanin, A.V.; Chalikov, D.; Young, I.R.; Savelyev, I. Numerical and laboratory investigation of breaking of steep two-dimensional waves in deep water. *J. Fluid Mech.* **2010**, *644*, 433–463. [CrossRef]

12. Trulsen, K.; Dysthe, K.B. *Action of Windstress and Breaking on the Evolution of a Wavetrain. Breaking Waves*; IUTAM Symposium: Sydney, Australia, 1991; pp. 244–249.

13. Galchenko, A.; Babanin, A.; Chalikov, D.; Young, I.; Haus, B. Influence of wind forcing on modulation and breaking of one-dimensional deep-water wave groups. *J. Phys. Oceanogr.* **2012**, *42*, 928–939. [CrossRef]

14. Fedele, F. Are rogue waves really unexpected? *J. Phys. Oceanogr.* **2016**, *46*, 1495–1508. [CrossRef]

15. Barbariol, F.; Alves, J.H.; Benetazzo, A.; Bergamasco, F.; Bertotti, L.; Carniel, S.; Cavaleri, L.; Chao, Y.Y.; Chawla, A.; Ricchi, A.; et al. Numerical modeling of space-time wave extremes using WAVEWATCH III. *Ocean Dyn.* **2017**, *67*, 535–549. [CrossRef]

16. Adcock, T.; Taylor, P.; Yan, S.; Ma, Q.; Janssen, P. Did the Draupner wave occur in a crossing sea? *Proc. R. Soc. A* **2011**, *467*, 3004–3021. [CrossRef]

17. Boccotti, P. *Wave Mechanics for Ocean Engineering*, 1st ed.; Elsevier: Amsterdam, The Netherlands, 2000; Volume 64.

18. Liu, P. A chronology of freaque wave encounters. *Geofizika* **2007**, *24*, 57–70.

19. Didenkulova, E. Catalogue of rogue waves occurred in the world ocean from 2011 to 2018 reported by mass media sources. *Ocean. Coast. Manag.* **2020**, *188*. [CrossRef]

20. Fedele, F.; Lugni, C.; Chawla, A. The sinking of the El Faro: Predicting real world rogue waves during Hurricane Joaquin. *Sci. Rep.* **2017**, *7*, 11188. [CrossRef] [PubMed]

21. Wada, R.; Waseda, T. Assessment of data-inherited uncertainty in extreme wave analysis. *J. Offshore Mech. Arct. Energy* **2020**, *142*, 021204. [CrossRef]

22. Datawell, B.V. *Datawell Waverider Reference Manual (WR-SG, DWR-MkIII, DWR-G)*; Datawell B.V.: Harlem, The Netherlands, 2009; p. 123. Available online: https://cdip.ucsd.edu/documents/index/gauge_docs/mk3.pdf (accessed on 18 June 2020).

23. Benetazzo, A.; Barbariol, F.; Bergamasco, F.; Torsello, A.; Carniel, S.; Sclavo, M. Observation of extreme sea waves in a space-time ensemble. *J. Phys. Oceanogr.* **2015**, *45*. [CrossRef]

24. Christou, M.; Ewans, K. Field measurements of rogue water waves. *J. Phys. Oceanogr.* **2014**, *44*, 2317–2335. [CrossRef]

25. Cavaleri, L.; Bajo, M.; Barbariol, F.; Bastianini, M.; Benetazzo, A.; Bertotti, L.; Chiggiato, J.; Davolio, S.; Ferrarin, C.; Magnusson, L.; et al. The October 29, 2018 storm in northern Italy–An exceptional event and its modeling. *Prog. Oceanogr.* **2019**, *178*. [CrossRef]

26. Fedele, F.; Herterich, J.; Tayfun, A.; Dias, F. Large nearshore storm waves off the Irish coast. *Sci. Rep.* **2019**, *9*, 15406. [CrossRef]

27. Barbariol, F.; Benetazzo, A.; Bertotti, L.; Cavaleri, L.; Durrant, T.; McComb, P.; Sclavo, M. Large waves and drifting buoys in the southern ocean. *Ocean Energy* **2019**, *172*, 817–828. [CrossRef]

28. Wang, D.; Mitchell, D.; Teague, W.; Jarosz, E.; Hulbert, M. Extreme waves under Hurricane Ivan. *Science* **2005**, *309*, 896. [CrossRef]

29. Cattrell, A.; Srokosz, M.; Moat, B.; Marsh, R. Can rogue waves be predicted using characteristic wave parameters? *J. Geophys. Res.* **2018**, *123*. [CrossRef]

30. Bleck, R. An oceanic general circulation model framed in hybrid isopycniccartesian coordinates. *Ocean Model.* **2002**, *4*, 55–88. [CrossRef]

31. Saha, S.; Moorthi, S.; Pan, H.; Wu, X.; Wang, J.; Nadiga, S.; Tripp, P.; Kistler, R.; Woollen, J.; Behringer, D.; et al. *NCEP Climate Forecast System Reanalysis (CFSR) Selected Hourly Time-Series Products, January 1979 to December 2010*; Research Data Archive at the National Center for Atmospheric Research, Computational and Information Systems Laboratory: Boulder, CO, USA, 2010. [CrossRef]

32. Saha, S.; Moorthi, S.; Wu, X.; Wang, J.; Nadiga, S.; Tripp, P.; Behringer, D.; Hou, Y.T.; Chuang, H.Y.; Iredell, M.; et al. *Updated Monthly. NCEP Climate Forecast System Version 2 (CFSv2) Selected Hourly Time-Series Products*; Research Data Archive at the National Center for Atmospheric Research, Computational and Information Systems Laboratory: Boulder, CO, USA, 2011. [CrossRef]

33. Mori, N. Freak waves under typhoon conditions. *J. Geophys. Res.* **2012**, *117*. [CrossRef]

34. Goda, Y. *Random Seas and Design of Maritime Structures*; World Scientific: Singapore, 2000; p. 443.

35. Mori, N.; Janssen, P. On kurtosis and occurrence probability of freak waves. *J. Phys. Oceanogr.* **2006**, *36*, 1471–1483. [CrossRef]

36. Scarfe, B.E.; Elwany, M.H.; Mead, S.T.; Black, K.P. *The Science of Surfing Waves and Surfing Breaks—A Review*; Scripps Institution of Oceanography Technical Report; Scripps Institution of Oceanography: La Jolla, CA, USA, 2003; p. 13.

37. Savage, J.; Tokmakian, R.; Batteen, M. Assessment of the HYCOM velocity fields during Agulhas return current cruise 2012. *J. Oper. Oceanogr.* **2015**, *8*, 11–24. [CrossRef]

38. Li, T.; Zheng, X.; Dai, Y.; Yang, C.; Chen, Z.; Zhang, S.; Wu, G.; Wang, Z.; Huang, C.; Shen, Y.; et al. Mapping near-surface air temperature, pressure, relative humidity and wind speed over mainland China with high spatiotemporal resolution. *Adv. Atmos. Sci.* **2014**, *31*, 1–9. [CrossRef]

39. Tahir, R.; Asim, M.; Jamil, S.; Shad, R.; Hayat, N.; Moaz, A.; Talha Akram, M.; Safyan, M. Comparison of reanalysis, analysis, and forecast datasets with measured wind data for a wind power project in Jhimpir, Pakistan. *IOP Conf. Ser. J. Phys.* **2018**, *1102*. [CrossRef]